International Journal of Solids and Structures 229 (2021) 111140

Contents lists available at ScienceDirect

International Journal of Solids and Structures

journal homepage: www.elsevier.com/locate/ijsolstr

Pop-up kirigami for stiff, dome-like structures

Maria Redoutey, Ariel Roy, Evgueni T. Filipov *

Department of Civil and Environmental Engineering, University of Michigan, Ann Arbor, MI 48109, USA

ARTICLE INFO

Article history:
Received 23 December 2020
Received in revised form 15 June 2021
Accepted 17 June 2021
Available online 24 June 2021

Keywords:
Origami
Kirigami
Infinitesimal mechanism
Pop-up structures
Positive Gaussian curvature

ABSTRACT

In architecture and engineering, surfaces with positive Gaussian curvature such as domes are used for their high stiffness-to-weight ratios and efficiency in enclosing a volume. These curved shapes are difficult to create due to time-consuming or scale-limited processes. In recent years, origami and kirigami have risen as viable routes for the rapid fabrication of complex surfaces from flat sheets; however, these methods typically lead to systems that are overly flexible due to their high number of degrees of freedom. In this paper, we present a design for a pop-up kirigami system that achieves symmetric, positive Gaussian curvature by taking advantage of an internal infinitesimal mechanism. The system is fabricated from flat sheets using a hexagonal pattern, and the sheets remain flat locally as the system deforms into a dome-like shape. We investigate the internal mechanism and deformation modes of the system, revealing the flexible mode that creates dome-like curvature. We discuss geometric variations of the system and illustrate the possible shapes that result from changing the initial pattern parameters. Finally, we demonstrate the high stiffness of the system that arises from restricting its one flexible mode in its final, dome-like shape. The proposed pop-up kirigami system offers a method for fabricating dome-like surfaces with potential applications as deployable enclosures, concave reflectors, and more.

1. Introduction

Surfaces with positive Gaussian curvature (dome-like shapes) have useful characteristics that make them applicable to a variety of fields. Such surfaces can be used to focus, refract, or attenuate signals, making them useful in the design of antenna reflectors, solar thermal systems, and auditoriums (Wulfrank et al., 2014; Girija Vallabhan and Panneer Selvam, 1985; Tibert and Pellegrino, 2002; Fonseca et al., 2018). In architecture and engineering, curved surfaces such as arches and domes make excellent structural systems due to their high stiffness to weight ratio. Domes made using material systems such as block masonry, poured concrete, and prestressed cables have been used for centuries as efficient roofs that can enclose large areas (Huerta, 2007; Pedreschi and Theodossopoulos, 2007; Pellegrino, 1992; Yuan et al., 2007).

It is a well-known phenomenon that adding curvature to a thin, flat sheet greatly increases its stiffness (Pini et al., 2016). Any surface created from a flat sheet without stretching or tearing has zero Gaussian curvature; such surfaces are classified as developable (Massey, 1962). It follows that introducing double curvature to a developable surface would be desirable; however, achieving positive Gaussian curvature from a flat sheet is difficult because it requires stretching, shrinking, crumpling, or tearing the sheet (Callens and Zadpoor, 2018; Modes et al., 2011). Instead, doubly curved surfaces are typically fabricated using processes such as casting, molding, additive manufacturing, or assembly from individual pieces. These processes have several drawbacks: casting materials such as concrete is a slow process and often relies on extensive formwork; molding and additive manufacturing are limited by scale and material while also requiring internal support; and assembling a structure from individual pieces leads to complicated and expensive construction requirements.

In recent years, origami has emerged as a way to rapidly assemble complex structural geometries from flat sheets (Filipov et al., 2015; Schenk and Guest, 2016). Foldable structures inspired by origami and designed using engineering principles can be deployed quickly from compact or stowed configurations (Zirbel et al., 2015; Thrall and Quaglia, 2014; Lee and Gattas, 2016). Origami structures are also scale independent, viable at the microscale (Leong et al., 2008; Zhu et al., 2020; Hawkes et al., 2010; Kuribayashi et al., 2006) to human- and building-scale (Filipov et al., 2019; Del Grosso and Basso, 2010).

Several origami methods have been explored to approximate curved surfaces, as reviewed by Callens and Zadpoor (2008). Periodic tesselations, such as the Miura-ori pattern, can be deformed out-of-plane into surfaces with nonzero Gaussian curvature if the

* Corresponding author.
E-mail address: filipov@umich.edu (E.T. Filipov).

https://doi.org/10.1016/j.ijsolstr.2021.111140
0020-7683/

flat facets of the sheet, or *panels*, are allowed to bend (Schenk and Guest, 2013; Dudte et al., 2016). Variations on the Miura-ori pattern have been designed to approximate complex curvatures while maintaining rigid folding characteristics, but the resulting structure remains flexible because of the possibility for bending (Feng et al., 2020). Concentric pleating, as seen in the origami hypar, can also result in negative Gaussian curvature (saddle shape), but this technique also requires panels to bend and twist (Demaine et al., 2011; Filipov and Redoutey, 2018). Tachi's origami bunny (Tachi, 2010; Demaine and Tachi, 2017) uses a tucking technique to achieve highly complex surfaces with nonzero Gaussian curvature, but this method is only possible with extremely thin materials and quickly becomes untenable as systems are scaled up. Kirigami methods, which allow for cutting of material, have been explored as well. Curved kirigami surfaces often require a nonuniform tesselation pattern (Martin, 2015) and do not lead to a structurally robust system (Cho et al., 2014). A kirigami core structure with spherical curvature has been demonstrated, but its stiffness properties have not been explored (Nojima and Saito, 2006). In summary, creating surfaces with curvature, especially dome-like curvature, from a flat sheet is a unique challenge that often requires significant panel deformation, infinitesimally thin materials, or nonuniform cutting and folding patterns. Furthermore, it is difficult to reach high stiffness using these origami and kirigami methods because thin sheets are prone to bending and folding. Due to these flexible deformation modes, origami systems need a large number of constraints to restrict movement and create a stiff structure.

In this paper, we present a pop-up kirigami system that deforms into a surface with dome-like curvature while the panels remain near to flat. The system begins as a kirigami structure with many flexible modes. As it deforms into a shape with positive Gaussian curvature, only one flexible mode remains; when that mode is restricted, the structure gains high stiffness. We show that the pop-up kirigami can accommodate thickness, lending it to future exploration as a system made of structural materials. The structure's pattern is a repeating array of hexagons and trapezoids, beginning from two flat sheets that have been cut and fastened together. Its ability to achieve positive Gaussian curvature is due to an intrinsic infinitesimal mechanism that leads to *synclastic* (dome-forming) behavior.

This paper introduces and explores the properties of the pop-up structures and is organized as follows: In Section 2, we define the system geometry, including how thickness can be incorporated for practical designs. The intrinsic properties of the system, including the infinitesimal mechanism that allows for the dome-like curvature deformation, are discussed in Section 3. Next, we explore the possible geometric variations of the system and the effects of the pattern geometry on the resulting shape (Section 4). Finally, in Section 5 we demonstrate the stiffening properties of the resulting structure.

2. Geometric definition

The inspiration for this system is a pop-up kirigami penguin toy made by Japanese artist Haruki Nakamura (Fig. 1(a)) (Nakamura, 2016). In his work, simple internal springs (usually made of rubber bands) are prestretched and locked when the toy is flat and are released when the toy is dropped, making the toy pop up into its 3D shape. We were intrigued by the structure of these toys because they begin as flat sheets and pop up into a 3D structure, a feature

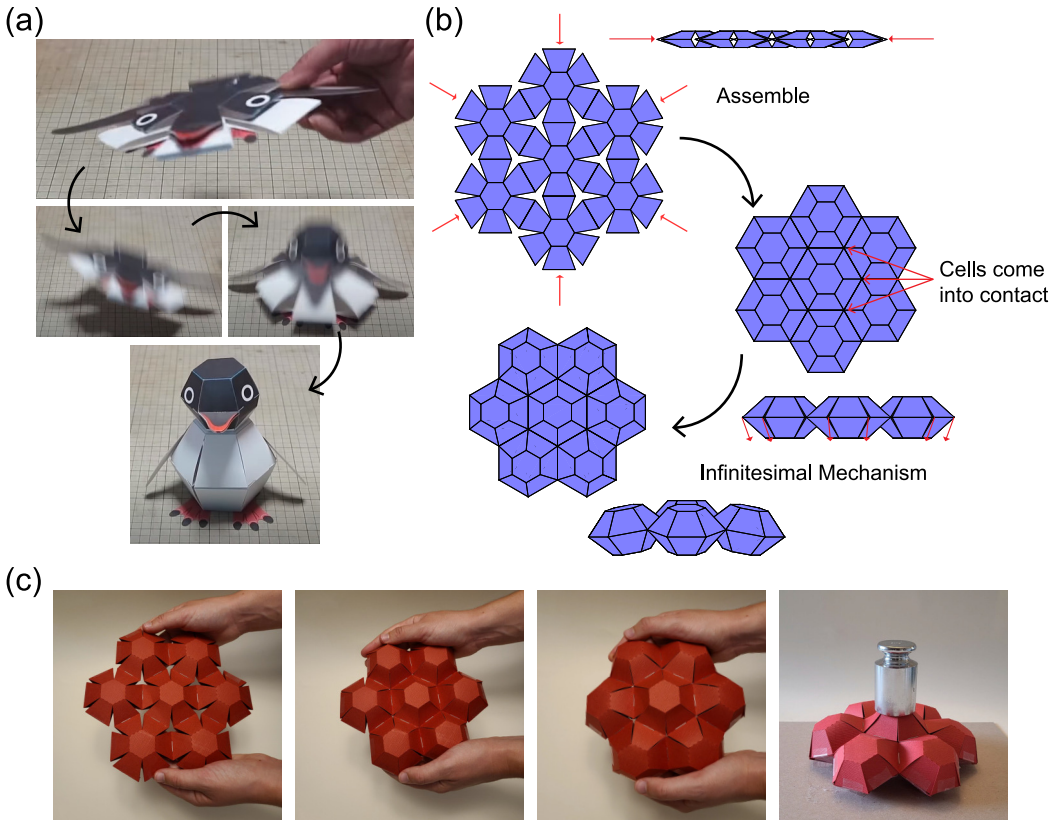

Fig. 1. (a) The pop-up kirigami penguin by Haruki Nakamura inspired the structure presented in this paper (Nakamura, 2016) (Images used with permission of the artist). (b) Pop-up kirigami structure in flat state, assembling into 3D array, and deforming into a dome-like structure. (c) Paper prototype of pop-up structure, shown in flat, assembled, and curved states. The prototype has a mass of 17 grams and supports a 500 g load with no noticeable deformation.

that is widely sought after in origami and kirigami engineering, especially for self-assembly at small scales (Bassik et al., 2009; Zhang et al., 2015). The penguin body (which holds the internal spring mechanism) is a cell constructed from two sheets of paper cut into a central hexagonal panel and six surrounding trapezoidal panels, which are fastened together along their outer edges (Maker, 2017). Our design is an array made up of these cells connected along those same outer edges, so that in places, four trapezoidal panels meet along one crease line. The result is a structure that can "pop up" into 3D as shown as the assembly step in Fig. 1(b). Here, we do not explore the internal spring mechanism and instead rely on external forces for the pop-up motion. In practice, a cable connected around the perimeter of the structure could be tightened to provide a radially confining force for assembly.

2.1. Planar geometric definition

The base of the pop-up system presented in this paper is a single cell made of two sheets cut into hexagonal and trapezoidal panels and connected along the bottom trapezoid edges. The pattern geometry of a cell is determined by the panel angle, γ and the panel length, L (Fig. 2(a)). In this paper, we assume the hexagon side length is always equal to 1 and scale all other units from this value. The possible range of the panel angle γ is $0 \leqslant \gamma < 30^\circ$. The assembled (3D) shape of a single cell is defined by the folding angle between two trapezoidal panels, θ, along with the trapezoid dimensions γ and L. The range of θ depends on γ; a pattern with a larger γ has a smaller range of θ (Fig. 2(b)). When $\gamma = 30^\circ$, the pattern cannot assemble into a 3D shape and remains a flat sheet. We define the folding angle when the cell is closed as the closed angle θ_c. The closed angle can be computed from the panel angle as: $\theta_c = 2\cos^{-1}(\tan(\pi/3)\tan(\gamma))$.

Individual cells are tessellated to create a larger cellular structure. The smallest of these structures has seven cells, and larger structures (with nineteen cells, thirty-seven cells, etc.) are made by adding cells radially outward from the center cell. In this and the following section, we primarily focus on the properties and behavior of a sample geometry of the seven-cell structure where $\gamma = 20^\circ$ and $L = 1.5$; in Section 4, we explore variations in γ, L, and the number of cells.

2.2. Modified design with thickness

A critical challenge of designing and creating practical origami and kirigami structures is accommodating the thickness of conventional materials (Tachi, 2016; Lang et al., 2018; Zirbel et al., 2013). In this subsection, we introduce a modified design of the pop-up kirigami structure that can accommodate finite thickness. The design adds thickness on both sides of the initially flat planes of the panels. To allow for folding without restricting the kinematics, we implemented a hinge-shift technique, which moves the rotational hinges to the edges of the panels (Lang et al., 2018) (Fig. 3(a)). The structure with thickness can fully assemble from flat into 3D with the addition of an angled cut along the bottom edge of each trapezoidal panel, as shown in Fig. 3. The angle of the cut β depends on the panel angle as: $\beta = \tan^{-1}[\tan[\pi/2 - \cos^{-1}(\sqrt{3}\tan\gamma)]\cos\gamma]$. This modification with an angled cut applies for any thickness and any geometric definition of the cell. The angled cut allows for uninhibited rigid folding kinematics, where the adjacent cells come into contact only when the cell is fully closed.

We fabricated a prototype with thickness using foam board (Fig. 3(c)). The geometric parameters of the prototype are $\gamma = 20^\circ$, hexagon side length $= 1''$, $L = 1.5''$, and thickness $t = 3/16''$. The angled cut allows for the cells to fully assemble into the 3D shape, and the structure can deform into a dome-like shape, similar to the paper prototypes.

3. Intrinsic properties of pop-up system

In this section, we used the bar and hinge method to simulate the pop-up system and explore several interesting intrinsic properties. We first investigated the internal mechanism of the seven-cell structure (Section 3.2). Next, we utilized the bar and hinge method to simulate the system assembling from flat to 3D and deforming into a dome-like shape (Section 3.3). Finally, we conducted an eigenvalue analysis to confirm the existence of an infinitesimal mechanism and explore other modes of deformation (Section 3.4).

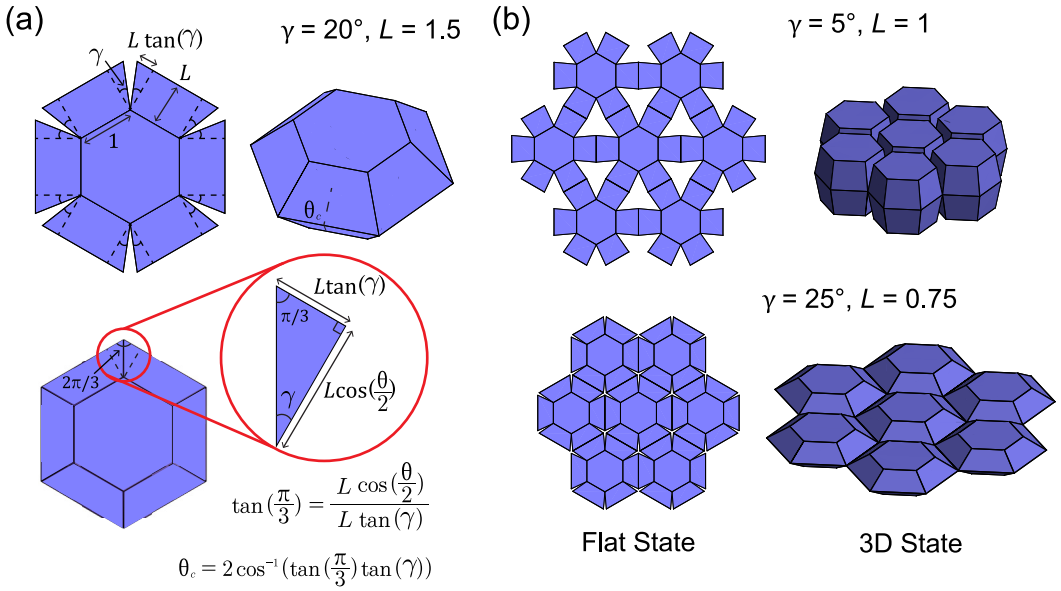

Fig. 2. (a) Geometry of a unit cell with $\gamma = 20^\circ$ and $L = 1.5$. The angle between two trapezoidal panels connected along their bottom edges is the folding angle θ, and when the cell becomes closed it is defined as θ_c. (b) Two examples of the seven cell structure with different geometries.

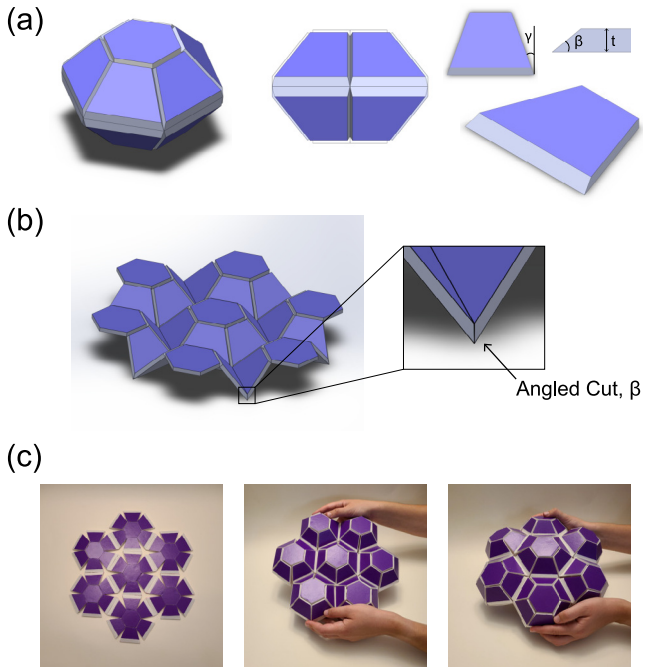

Fig. 3. (a) A 3D model of a single cell with the angled cut β shown on the trapezoidal panels. (b) A subset of the seven-cell system modeled with thickness. The angled cut β allows for the cells to fully assemble. (c) A prototype of the pop-up structure fabricated with foam board (thickness = 3/16″).

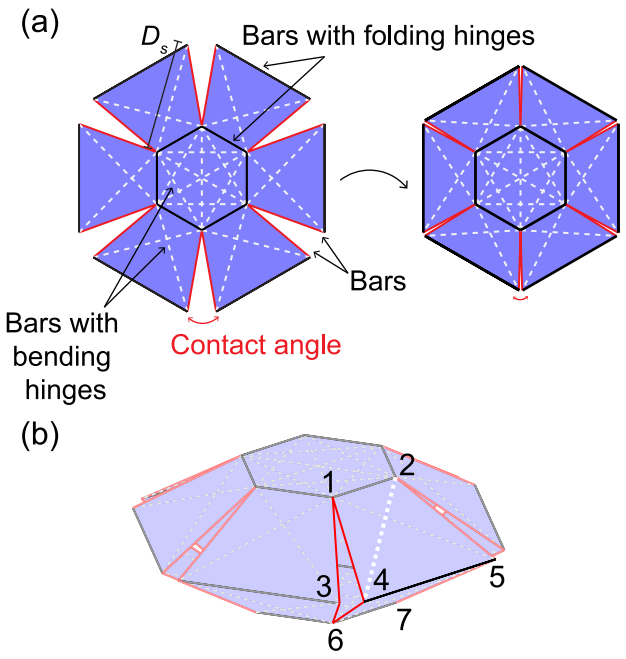

Fig. 4. (a) Bars are used to capture the in-plane stiffness of the trapezoidal and hexagonal panels. Bending hinges (shown in dashed lines) capture bending stiffness of the panels. Folding hinges (black lines) represent the folding stiffness of the crease lines. The bars on the sides of the trapezoidal panels (red lines) are the only ones that do not have bending or folding hinges defined along them. (b) Folding, bending, and panel contact are all modeled used rotational springs. The angle of a spring is calculated using adjacent triangles: for the folding hinge shown, we use two sets of symmetric triangles 5-4-1 & 5-4-6 and 4-5-2 & 4-5-7; for the bending hinge, the triangles 2-4-1 and 2-4-5; and for the contact spring, the triangles 1-6-3 and 1-6-4.

3.1. Bar and hinge model for pop-up system

The bar and hinge method models origami and kirigami structures as pin-jointed assemblages (Schenk and Guest, 2016). It can capture in-plane deformations, crease folding, and panel bending seen in origami structures (Liu and Paulino, 2017; Filipov et al., 2017; Liu and Paulino, 2018). Our bar and hinge model is based on the MERLIN2 origami modeling package because it can perform large-displacement, highly nonlinear analyses (Liu and Paulino, 2018). With the bar and hinge model, the panels of the kirigami structure are replaced by bars outlining the perimeter of the panels and spanning across the panel diagonals. These bars capture in-plane stretching and shearing deformations. Folding and bending deformations (which occur at the crease lines of the kirigami structure and within the panels, respectively) are modeled using torsional springs defined along the appropriate bars, as illustrated in Fig. 4(a). For a more detailed discussion of the formulation of the bar and hinge model and the MERLIN2 package, please see Liu and Paulino (2017) and Liu and Paulino (2018).

The stiffness of the system, used to formulate equilibrium equations and solve for a force or displacement response, is comprised of contributions from these components, as well as contact springs that simulate adjacent panels coming into contact. The total strain energy U of the system is a sum of these four contributions:

$$U = U_S + U_F + U_B + U_C$$

where U_S is the strain energy due to bar stretching, U_F is the energy due to crease folding, U_B is the energy due to panel bending, and U_C is the energy due to panel contact. These strain energy derivations are presented in detail in Liu and Paulino (2017) and Zhu and Filipov (2019).

We model all bars, including those with torsional springs, using a material with Young's modulus $E = 10^8$, thickness $t = 0.01$, and Poisson ratio $\nu = 1/3$. We use these arbitrary units of realistic relative magnitudes to demonstrate the fundamental characteristics of the pop-up structures. The axial (stretching) bar stiffness K_S is EA/L, where A is the bar cross-sectional area and L is the bar length. Formulations of bar cross-sectional areas for quadrilateral panels, including skewed (parallelogram) panels, have been established in the literature (Filipov et al., 2017), and a general approximation for polygonal panels has also been proposed (Liu and Paulino, 2018). Our system includes hexagonal and trapezoidal panels, which require new bar area definitions for accurate modeling of their in-plane stiffness. We derive appropriate bar areas and present them in Appendices A and B for hexagonal and trapezoidal panels respectively.

The panel bending stiffness K_B depends on the material parameters E, t, ν and the panel geometry, as follows:

$$K_B = \left(0.55 - 0.42\frac{\Sigma\alpha}{\pi}\right)\frac{Et^3}{12(1-\nu^2)}\left(\frac{D_S}{t}\right)^{1/3}, \quad (1)$$

where $\Sigma\alpha$ is the sum of the outer angles of the panel corners adjacent to the shortest diagonal and D_S is the length of the shortest diagonal bar (Filipov et al., 2017). For trapezoidal panels, $\Sigma\alpha = \pi$ and $D_s = \sqrt{L^2 + (1 + L\tan\gamma)^2}$. For hexagonal panels, $\Sigma\alpha = 3\pi/2$ and $D_s = \sqrt{3}$. The magnitudes of $\Sigma\alpha$ and D_s do not significantly affect the simulation results. Torsional springs with stiffness K_B are defined at all bending hinges in the structure. For example, a bending hinge is modeled on the bar connecting nodes 2 and 4 in Fig. 4; the angle between the triangles 2-4-1 and 2-4-5 defines the hinge. The stiffness of the fold lines K_F is defined as $K_B/1000$ in order to simulate a structure with panels that are stiff and folds that provide near zero contribution to the rigidity of the structure. Two torsional springs, each with stiffness $K_F/2$, are defined at all folding hinges in the structure. The angles of the folding hinges are defined by two sets of adjacent triangles. Using two sets of sym-

metric triangles to define the hinge angle allows us to capture the displacement of all nodes adjacent to the folding hinge. An example of a set of folding hinges is along the crease line connecting nodes 5 and 4 in Fig. 4(b). One hinge is defined by the angle between the triangles formed by nodes 5-4-1 and 5-4-6; the other is defined by the symmetric triangles 4-5-2 and 4-5-7.

An important and challenging aspect of origami modeling is capturing when panels come into contact (Zhu and Filipov, 2019). To avoid panel intersections, we implement a simplified contact model using a penalty function applied to a torsional spring (Liu and Paulino, 2017). Contact torsional springs were defined between adjacent trapezoidal panels with axes spanning between the top and bottom sheets. For example, a contact spring is defined connecting nodes 1–6 in Fig. 4(b). The rotation of the spring is calculated as the angle between the triangles formed by nodes 1-6-3 and 1-6-4, so that as nodes 3 and 4 approach each other, contact is engaged. The initial stiffness of the contact hinge is $K_C = 20 * K_F$ and the stiffness increases toward infinity as the distance between nodes 3 and 4 approaches zero. The initial value for K_C is low because when contact is not engaged, neither folding hinges nor contact springs contribute to the stiffness of the system. After contact, the contact springs do contribute to the system stiffness, so K_C increases towards infinity. This increase in stiffness avoids panel intersection and simulates the effect of the panels coming into contact.

3.2. Mechanism analysis

Through informal experimentation with paper models of the pop-up structure, we observed that the system has the ability to deform into a shape with dome-like curvature (Fig. 1(c)). While the unassembled structure has many flexible modes, when the structure is assembled into 3D, the dome-forming mechanism is the only flexible motion. Using the bar and hinge method described in Section 3.1 along with several resources on the analysis of internal mechanisms, we verified that this motion is the result of a single infinitesimal mechanism.

Pin-jointed assemblages (such as a structure modeled using bars and hinges) can be described mechanically in terms of the number of inextensional mechanisms (m) and states of self-stress (s) that are possible for the structure (Calladine and Pellegrino, 1991). A mechanism is defined as a displacement that does not cause internal forces to develop in the structure (excluding rigid body motions of the full system in space). A state of self-stress is a condition where nonzero internal forces in a structure can exist in equilibrium without the application of external forces. The quantities m and s are also referred to as the degrees of kinematic (m) and static (s) indeterminacy (Tarnai, 2001; Pellegrino, 1988; Kangwai and Guest, 1999). In certain cases, activating a structure's state of self-stress leads to a stiffening effect in one or more of its mechanisms. These cases are known as *infinitesimal mechanisms,* in contrast to finite mechanisms, which allow for large nodal displacements with no stiffening (Pellegrino and Calladine, 1986).

The equilibrium and kinematic equations of a pin-jointed structure involve the following quantities: the internal bar forces **t**, the external loads applied at the joints **f**, the joint displacements **d**, and the bar elongations **e**. These quantities are related to each other by the equilibrium matrix **A**:

$$\mathbf{At} = \mathbf{f},$$

and its transpose, the compatibility matrix $\mathbf{B} = \mathbf{A}^{\mathbf{T}}$:

$$\mathbf{Bd} = \mathbf{e}.$$

The quantities m and s are related to the number of bars (b), non-support joints (j), and support reactions (k) in a structure through an extension of Maxwell's rule, which is typically used to determine a structure's degree of static indeterminancy: $s - m = b - 3j + k$ (Pellegrino and Calladine, 1986). However, the exact values of m and s for a given structure cannot be found simply by counting the bars and joints. They require computing the four vector subspaces of the structure's equilibrium matrix: the null space, left null space, column space, and row space. The null space of the equilibrium matrix contains the structure's independent states of self-stress (and therefore s), and the left null space gives the mechanism displacements **D** (and therefore the number of mechanisms m). The column space identifies the non-redundant bars of a structure, essentially describing the statically determinate structure that would result if the redundant bars were removed. The row space gives the set of geometrically compatible bar elongations.

Pellegrino and Calladine developed an algorithm that evaluates whether a pin-jointed structure's internal mechanisms are infinitesimal or finite (Calladine and Pellegrino, 1991; Pellegrino and Calladine, 1986). The algorithm involves calculating the product force vectors **P** associated with a particular mechanism, which give the loads that occur at the joints as the structure moves into the mechanism displacement and is no longer in equilibrium under zero external load. A modified equilibrium matrix **A'** is then constructed to include these product force vectors and describe the new equilibrium state: $\mathbf{A}' = [\mathbf{A}|\mathbf{P}]$. If this modified equilibrium matrix is full rank, the mechanism in question is infinitesimal. An additional check for positive definiteness of $\mathbf{A}'$ verifies the stability of the infinitesimal mechanism.

Following the algorithm approach, we discovered that the seven-cell pop-up kirigami structure has one infinitesimal mechanism. Using the bar and hinge model, we obtained the structure's equilibrium matrix and its four vector subspaces. The left null space contains one set of mechanism displacements, thus giving a value of $m = 1$. When the mechanism displacements **D** are applied to the structure, the resulting shape resembles a dome, as we expected and as shown in Fig. 1. We then followed the procedure outlined in the literature to compute the product force vectors and assemble the modified equilibrium matrix $\mathbf{A}'$, we verified that it is full rank, and performed the stability check. The seven-cell structure has 432 degrees of freedom and 18 of them are restrained at the bottom center hexagonal panel. The structure has 714 bars, and the equilibrium matrix **A** has dimensions (714×432). The modified equilibrium matrix **A** has dimensions (414×413), and there are 301 possible independent states of self-stress ($s = 301$). These quantities, along with $m = 1$ for the structure, satisfy the extension of Maxwell's rule. The result of the algorithm confirms that the mechanism is infinitesimal. This means that after an initial (infinitesimal) displacement into the dome-like shape, all energy contributions of the system (stretching, folding, bending, and contact) are engaged.

3.3. Achieving dome-like curvature

The mechanism analysis presented in Section 3.2 reveals that the pop-up system has the ability to achieve dome-like curvature, thanks to an internal infinitesimal mechanism. In this section, we study the system as it follows the infinitesimal mechanism and deforms into a dome-like shape. We used the bar and hinge method described in Section 3.1 to perform a two-step, displacement controlled analysis to simulate the structure as it assembles from flat and subsequently deforms. The first step (assembly) runs until the contact angle between the trapezoidal panels is sufficiently small ($< 3^\circ$). This angle limit ensures that the spaces between cells are nearly closed and that adjacent trapezoidal panels are engaging the contact hinges. The second step (mechanism)

deforms the structure into a dome-like shape using a follower displacement applied at the 12 nodes along the outer perimeter of the structure and runs until the maximum bar strain (regardless of whether in tension or compression) exceeds 0.01%. This threshold was chosen to emulate realistic strain values that structural materials can experience without failure. The magnitudes of the bar strains are representative of the forces required to deform the structure into a dome-like shape. Since the dome-forming motion is an infinitesimal mechanism, the strain (and force) magnitudes are low, but not zero (as would be the case for a finite mechanism). The structure has the ability to curve more if higher strains are allowed.

Fig. 5 illustrates the two-step analysis for the pop-up structure. We use two metrics to quantify how the geometry of the structure changes during the analysis (shown in Fig. 5(a)): the *clear rise*, defined as the vertical distance from the bottom nodes of the outer cells to the bottom nodes of the center cell, and the *clear span*, the horizontal distance between bottom nodes of opposite outer cells. During the assembly step, the clear rise remains zero and the clear span shortens as the structure comes together into its 3D shape. Bar strains remain near zero during this step. During the mechanism step, the system takes on the curved shape of the infinitesimal mechanism discussed in Section 3.2. At this point panel contact is engaged and the bar strains increase as a result. As the strains increase, the clear span decreases and the clear rise increases. A more descriptive parameter that we use to understand the curvature of the structure is the ratio of clear rise to clear span. The ratio increases during the mechanism step as the structure becomes more curved.

For the seven-cell system with $\gamma = 20^\circ$ and $L = 1.5$, the clear span shortens from 11 to 8 during the two-step analysis. During the mechanism step, the clear rise grows to 0.9, resulting in a final clear rise to clear span ratio of 0.11. As the clear rise increases and the clear span decreases during the deformation, the structure begins to take the shape of a spherical cap. A practical limit to the clear rise to clear span ratio is 0.5, corresponding to a hemisphere.

The mechanism displacements can occur without significant panel bending, as can be shown using the two-step analysis. During the analysis, the bending angles of all panels remain less than 3° while the majority of the bending angles remain below 1° (Fig. 6). These small bending angles confirm that the panels remain nearly flat, especially when the infinitesimal mechanism is first

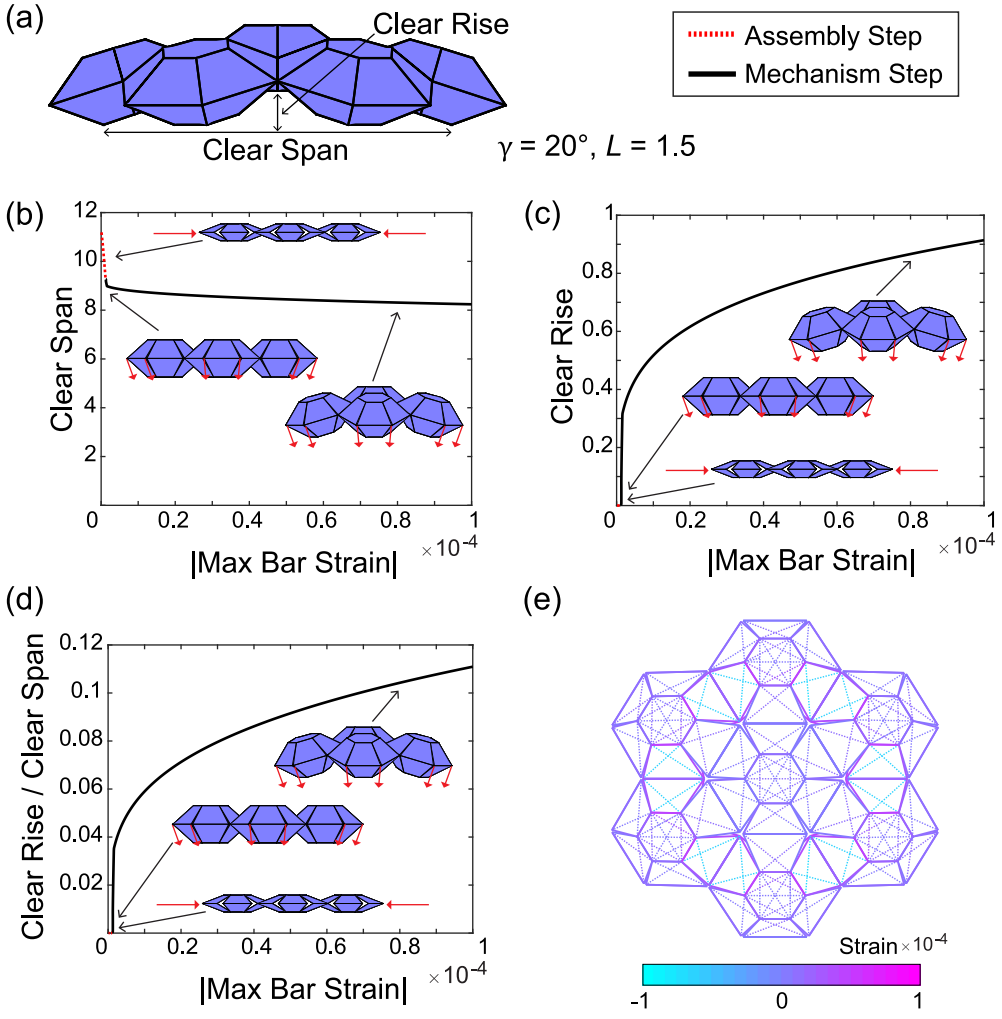

Fig. 5. (a) We use two metrics to quantify the change in geometry of the system during the two-step analysis: clear rise and clear span. We define the clear rise as the vertical distance from the bottom nodes of the outer cells to the bottom nodes of the center cell, and the clear span as the horizontal distance between bottom nodes of opposite outer cells. (b)–(c) As bar strains increase during the analysis, the clear span decreases and the clear rise increases. (d) The ratio of clear rise to clear span is used to describe the increasing curvature of the structure during the analysis. (e) Distribution of bar strains at the end of the two-step analysis.

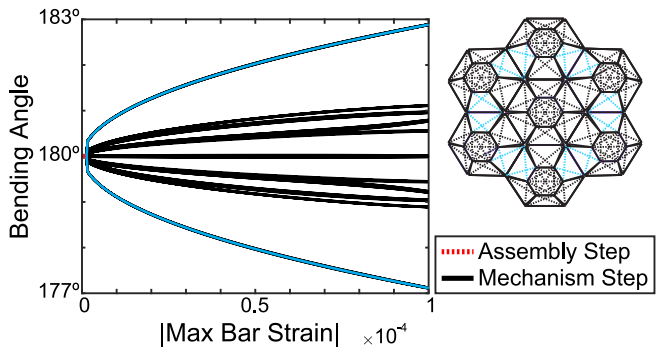

Fig. 6. Small bending angles develop in the structure during the two-step analysis. Most of the angles are less than 1°. Some panels experience bending angles up to ≈ 3° (highlighted in blue).

applied. Since the mechanism is infinitesimal, small stretching and bending energies develop in the panels as the analysis progresses and displacements become larger.

3.4. Eigenvalue analysis

In addition to the mechanism analysis, we investigated the eigenvalues and eigenmodes of the pop-up structure. The eigenmodes provide information on the structure's infinitesimal mechanism, deformation characteristics, and self-stiffening property. The eigenvalues and modes are found using the equation $\mathbf{K}\phi_i = \lambda_i\phi_i$, where $\mathbf{K}$ is the structure's full stiffness matrix obtained from the bar and hinge model, ϕ_i is the i^{th} eigenmode vector, and λ_i is the i^{th} eigenvalue. The magnitude of an eigenvalue λ scales directly with the energy required to deform a structure into the shape described by the corresponding eigenmode. A higher eigenvalue indicates a stiffer (more energetically expensive) deformation. An eigenvalue of zero indicates a deformation that does not produce any internal forces in a structure – either a rigid body motion or an internal mechanism.

The eigenvalues and eigenmodes of the pop-up structure in various configurations are shown in Fig. 7. In addition to the flat structure, we conducted the eigenvalue analysis for the assembled structure (Fig. 7)) and curved structure (Fig. 7(d)). These geometries were found using the two-step analysis described in Section 3.3. Due to the change in geometry, the global stiffness of the structure is different for each of these configurations, therefore the eigenvalues also change. We also explored how the eigenvalues of these configurations change when the nodes of adjacent cells are connected (Fig. 7(c) and (e)). For the connected cases, the nodes that come into contact during assembly are connected by bars with high stiffness. The connected design represents a practical scenario where the individual cells of the structure are connected after assembly. This connected scenario accounts for the increased stiffness due to contact which can be captured by the large displacement analyses (Fig. 5), but is not captured in the infinitesimal eigenvalue simulations without connections.

The first six eigenvalues of the flat (unassembled) structure are zero, and they represent the six rigid body motions in space. The next eigenvalue (λ_7) is very close to zero, meaning it is an internal mechanism. The 7th eigenmode of the flat structure is the dome-like curved shape, as we found in the mechanism analysis (Section 3.2). The 8th eigenmode is the assembly motion, where the structure "pops up" from flat to 3D. The 9th eigenvalue is representative of the energy of a higher mode, where some cells are squeezed.

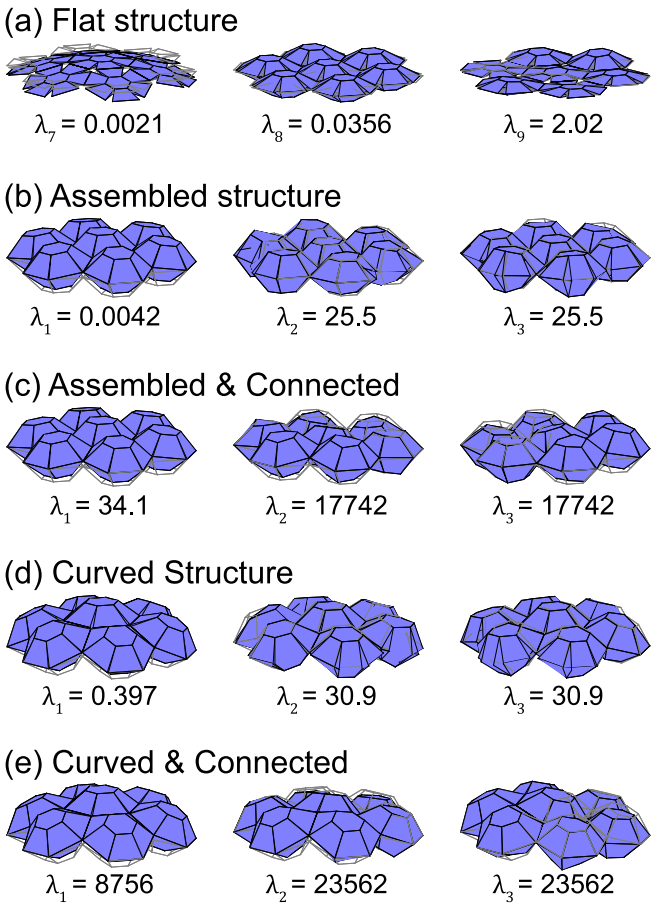

Fig. 7. Eigenvalues and eigenmodes of the pop-up structure. (a) Modes of the flat, unassembled structure. Eigenvalues $\lambda_1 - \lambda_6$ of this configuration are the rigid body motions in space. The next eigenvalue λ_7 is ≈ 0, indicating that it is an internal mechanism. (b) Modes of the assembled structure with the outer perimeter constrained. The eigenvalue corresponding to the infinitesimal mechanism λ_1 remains near zero. (c) Connection bars are added to the nodes which come into contact for the assembled structure, increasing the eigenvalues. The first eigenvalue λ_1 remains small compared to λ_2 and λ_3. (d) Modes of the structure after it is deformed into a dome-like shape. The first eigenvalue λ_1 is again near zero, reflecting the infinitesimal mechanism, and the other modes remain relatively flexible. (e) Modes of the curved structure with connections. All eigenvalues are high, indicating a stiff structure.

For all configurations other than flat, additional boundary constraints were included to restrict the structure's rigid body motions in space; thus, in Fig. 7(b)–(e) the eigenvalues begin at λ_1. For these configurations, the first eigenvalue λ_1 is significantly lower than λ_2 and λ_3. The jump between eigenvalues indicates a large increase in stiffness between the modes; the first eigenmode (which resembles the dome-like shape) is significantly more flexible than other modes. The first eigenvalues λ_7 and λ_1 in parts (a, b, d) of Fig. 7 represent the infinitesimal mechanism and are much lower than the subsequent eigenvalues. These eigenmodes require only folding along the crease lines and minor bending in the panels. In contrast, some of the eigenvalues for the connected structures are several orders of magnitude higher because they require stretching and shearing of the sheet. By itself, deforming the structure into the curved shape only results in a modest increase in eigenvalues because the infinitesimal eigenmodes can still exhibit self-intersection and local squeezing deformations (λ_2 and λ_3 of Fig. 7 (d)). When we place a perimeter boundary and internal connec-

tions (representing adjacent panels in contact) in the structure, all eigenmodes are significantly stiffened as shown in Fig. 7(e). These eigenvalue simulations show that the flexible infinitesimal mechanism can be used to assemble the kirigami into the dome-like shape which can then be stiffened by internal contacts and perimeter constraints.

4. Geometric properties from parameter variations

We performed a parametric study to compare the final dome-like shapes of the kirigami structures with different panel angles γ, panel lengths L, and number of cells. To compare across all geometric variations, we normalized the clear rise and clear span (defined in Section 3.3) by dividing by the *closed span*, the horizontal dimension of the structure in its 3D (fully assembled) state. The *clear volume* is the volume underneath the structure, calculated using the volume of a spherical cap ($V = 1/6\pi h(3a^2 + h^2)$) where the height h is equal to the clear rise and the base radius a is equal to half of the clear span. The *enclosed volume* is the volume within all cells of the structure, and the *% clear volume* is the ratio of the clear volume to the total volume (clear plus enclosed). These metrics are illustrated in Fig. 8(a).

4.1. Changing γ and L

The two-step analysis described in Section 3.3 was conducted for structures with various panel angles ($\gamma = 10^\circ - 25^\circ$) and panel lengths ($L = 0.75, 1, 1.25, 1.5$). Shown in Fig. 8, these parameters

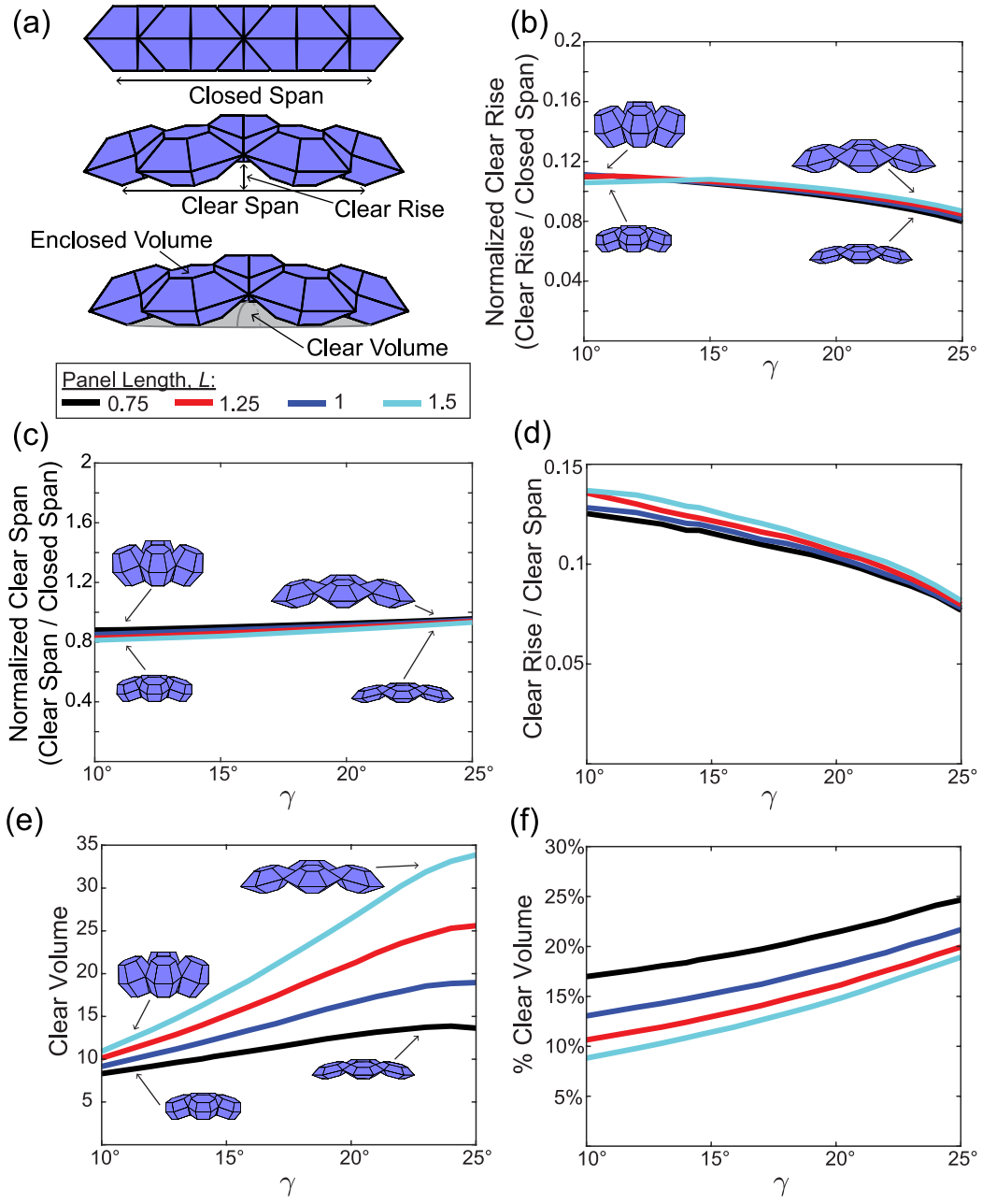

Fig. 8. (a) Geometric properties measured for the curved pop-up kirigami structures: closed span, clear rise, clear span, clear volume, and enclosed volume. (b) The normalized clear rise (clear rise/ closed span) plotted for various γ and L. Larger γ results in systems with smaller normalized clear rise. (c) Normalized clear span (clear span/ closed span) plotted for various γ and L. Larger normalized clear spans result from systems with larger γ. (d) The ratio of clear rise to clear span decreases as γ increases, and is mostly independent of L. (e) Larger L and γ result in structures with larger clear volumes. (f) Interestingly, structures with smaller L results in higher % clear volumes.

drastically influence the final appearance and geometric properties of the final shape. We found that the normalized clear rise and the normalized clear span depend only on γ, with little variation for different values of L. The normalized clear rise decreases as γ increases, while the normalized clear span increases slightly. (Fig. 8(b, c)). The clear rise to clear span ratio of all geometries ranges between 0.07 and 0.14. Many classical domes used in architecture have a clear rise to clear span ratio near to 0.5. One way to increase the clear rise to clear span ratio of the proposed kirigami structures is to add more cells, as discussed in Section 4.2.

Geometries with larger γ and L result in structures with larger clear volume, and for larger panel lengths an increase in γ leads to a more dramatic increase in clear volume (Fig. 8(e)). Interestingly, the relationship between % clear volume and L is flipped; a larger L gives a *smaller* % clear volume. This relationship indicates that we can construct a structure with a higher fraction of usable space to total occupied volume (larger % clear volume) using less material (smaller L).

4.2. Adding cells

In addition to the seven-cell system, we also studied a larger system with 19 cells. The nineteen-cell structure assembles and deforms into a dome-like surface in the same manner as the seven-cell version, as demonstrated by the bar and hinge simulations and physical prototypes (Fig. 9(a)). We were interested in whether adding cells would result in a more curved structure, and we use the clear rise to clear span ratio as a measurement of curvature. Fig. 9(b) shows that for a structure with $\gamma = 20^\circ$ and $L = 1.5$, when curved to reach the same bar strains, the nineteen-cell system reaches a higher clear rise to clear span ratio: 0.15 up from 0.11. This increase is a good indication that by continuing to add cells, our design could reach the curvature levels of typical domes found in architecture and structural engineering. Additionally, this structure has a clear volume of 214 in comparison to the clear volume of 24 for the seven-cell structure with the same geometric parameters. This is about a nine (8.9) times increase in usable clear volume for only about a three (2.7) times increase in the total material used to construct the structure.

5. Dome stiffness

To investigate the stiffness of the pop-up kirigami structure, we constrained the structure along the outer perimeter in the x-, y-, and z-directions and applied small vertical displacements ($\Delta = -0.1$) at the interior points where the cells meet (Fig. 10(a)). The bar and hinge method described in Section 3.1 was used to apply the displacement in 10 steps and calculate the resulting vertical forces (F) at the supports. The force–displacement relationship was linear in this range of deformation. A stiffness value representing the full structure was found using the relationship $K = \Sigma F/\Delta$.

Overall, we found that the stiffness of the curved structures mostly depends on γ, and the stiffness varies less significantly with L (Fig. 10(c)). To better understand the characteristics of the pop-up kirigami, we compare its stiffness with a curved sheet restrained on two edges with clear rise and clear span values averaged from the results in Section 4 and twice the material thickness of the kirigami panels (to account for the two sheets used in the pop-up structures). An analytical approximation for the stiffness of the curved sheet is found using Castigliano's theorem and provides a basepoint comparison for the stiffness values (Appendix C). The comparison shows that our structures, with any γ or L, are as stiff as a curved sheet made of material with 10 to 17.5 times the total pop-up kirigami thickness ($t_c = 10 * 2 * t$ to $t_c = 17.5 * 2 * t$). Because the bending rigidity of the sheet scales with t_c^3, the pop-up kirigami is in fact $\approx$ 1,000 to 5,000 times stiffer than a simple sheet supported only along two edges. The high stiffness is a result of the dome-like curvature and of the flexible deformation mode (the mechanism displacements) being restrained. As shown in Section 3.4, the curved structure only has one flexible mode, corresponding to the mechanism displacements. When this flexible mode is restrained, the structure gains high stiffness.

We also investigated the stiffness of the seven-cell structure with $\gamma = 20^\circ$ and $L = 1.5$ for different loading directions (Fig. 11). The loads were applied at the same six interior nodes as the previous analysis, and the load direction was changed in the x-z and x-y planes. The structure exhibits the highest stiffness in response to horizontal loads in the x-y plane. While there are three axes of

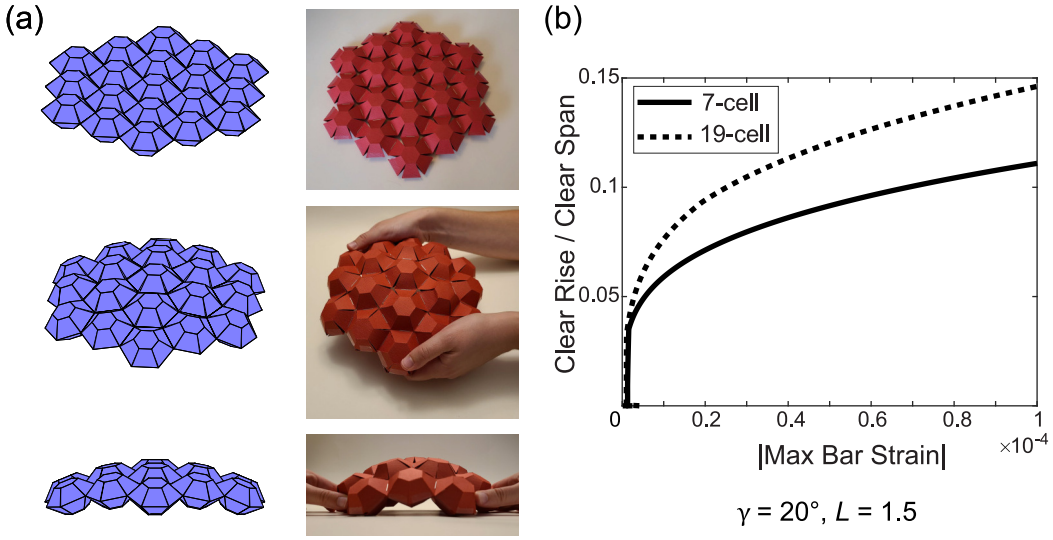

Fig. 9. (a) A nineteen-cell variant of the pop-up system, modeled with the bar and hinge method and as a paper prototype. (b) The clear rise to clear span ratio of the nineteen-cell system is larger than that of the seven-cell system with the same geometry when curved to reach the same magnitude of bar strains.

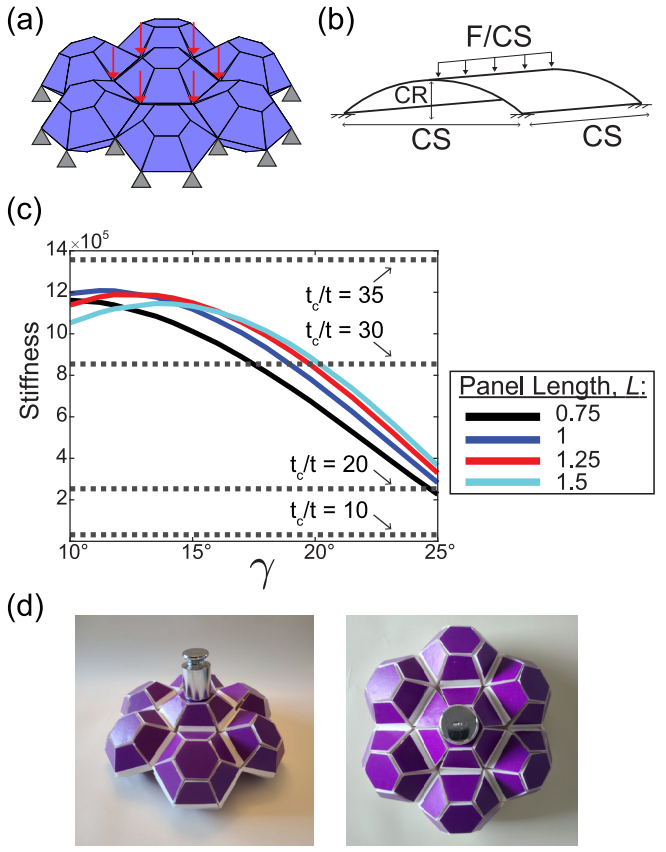

Fig. 10. (a) In the stiffness analysis, the outer perimeter was pinned and small vertical displacements were applied to the interior nodes of the structure. (b) An analytical solution for the stiffness of a curved sheet restrained along two edges is used as a basepoint for stiffness comparison. (c) The stiffness of the pop-up kirigami structures decreases as γ increases. For comparison, the stiffness of curved sheets with thickness t_c are shown in dashed lines, where t is the thickness of the pop-up kirigami. (d) From left to right: 7-cell paper structure (mass = 17 g), 19-cell paper structure (mass = 28 g), and 7-cell foam board structure (mass = 57 g). Each holds a 500 g load without a noticeable deformation.

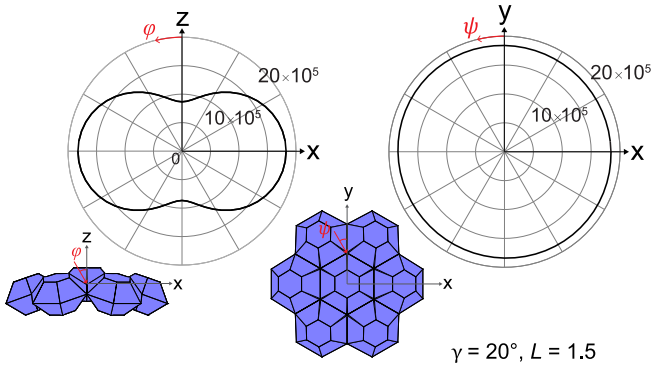

Fig. 11. The stiffness of the pop-up structure in the x-z and x-y planes shown as radial plots where the distance from the center indicates the stiffness magnitude. The angles ϕ and ψ represents the loading direction in a given plane. The structure exhibits the largest stiffness in the x-y plane (horizontal loading).

radial symmetry for the structure, the stiffness is uniform in all x-y directions, meaning there will be a high stiffness regardless of how horizontal loads are applied. When loaded vertically in the z-direction, the structure has about half the stiffness in comparison to the horizontal directions, but this stiffness is still high, as shown in Fig. 11. These results indicate that the pop-up structures are adaptable to loads that change directions, such as wind loads.

6. Conclusion

In this paper, we presented a design for a pop-up structure that achieves dome-like curvature from flat panels. The system starts with a kirigami-inspired pattern of two sheets, cut into hexagonal and trapezoidal panels and fastened to create an array of cells that assemble into a 3D structure. We demonstrated that the system can accommodate finite thickness and maintain nearly rigid panels as it deforms into a structure with positive Gaussian curvature. With this design, we have the potential to create large, dome-like structures from flat sheets, taking advantage of the simplified fabrication and rapid deployment that are made possible by origami and kirigami designs.

We identified the internal mechanism that leads to the formation of a dome-like curved shape and showed that the higher deformation modes of the structure become restricted as the curvature increases. We studied geometric variations of the structure by changing the panel angle γ and panel length L. Structures with smaller γ result in a higher clear rise to clear span ratio, a metric we use to describe curvature. When studying the volume of the systems, we found that structures with large γ and small panel length L result in more geometrically efficient designs that can enclose a larger volume for a smaller volume of total structure. We also found that by adding more cells, the shape trends towards the classic dome shape used in architecture. We showed that in the dome-like shape, the pop-up kirigami structure has only one flexible deformation mode, and a stiffness analysis showed that the dome-like shape makes the structure 1,000 to 5,000 times stiffer than a curved sheet with the same total thickness that is supported only along two edges. We also showed that the structure has high stiffness regardless of the loading direction. This system is the first self-stiffening kirigami structure that can deform into a dome-like shape, and has potential to be used for rapidly deployable enclosures, reflectors, architectural components, and other robust structures with dome-like curvature.

Declaration of Competing Interest

The authors declare that they have no known competing financial interests or personal relationships that could have appeared to influence the work reported in this paper.

Acknowledgments

The authors are grateful for the financial support provided by the SURE Program at the University of Michigan, the MCUBED program at the University of Michigan, the Defense Advanced Research Projects Agency (DARPA Grant No. D18AP00071) and the National Science Foundation (NSF CAREER #1943723). The paper reflects the views and opinions of the authors, and not necessarily those of the funding entities.

Appendix A. Bar area formulations for hexagonal panels

The hexagonal panels are modeled using the bar and hinge method with 15 bars, shown in Fig. A.1. Six bars connect the nodes along the perimeter of the panels and have bar cross-sectional area A_{ext}. Three bars with area A_{int1} connect the major diagonals of the hexagon, and six bars with area A_{int2} connect the shorter diagonals of the hexagon.

The bar areas were chosen such that the stretching and shearing behavior of the hexagonal panel matches the behavior of a block of material with length and width s, the side length of the hexagonal panel. The theoretical stretching stiffness of the block of material is

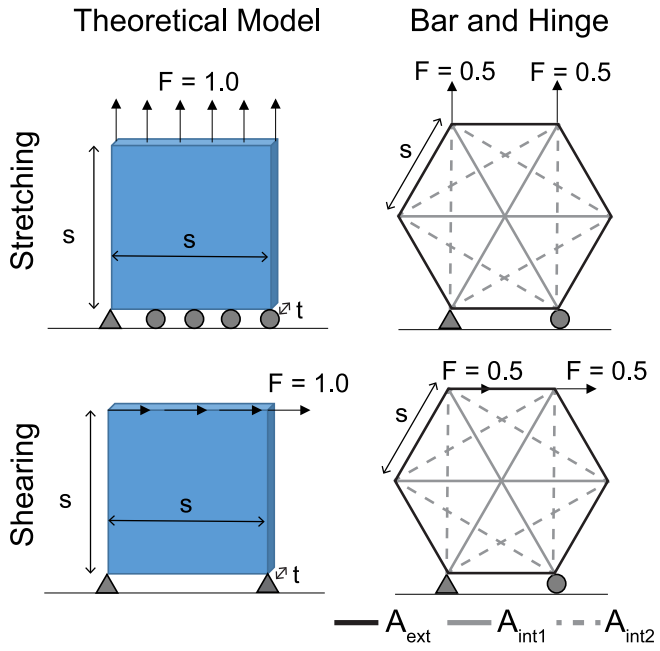

Fig. A.1. The stretching and shearing stiffness of the hexagonal panels was defined to match the stiffness of a square block of material with comparable dimensions.

$K = EA/L = Est/s = Et$. The theoretical shear stiffness is $K_{sh} = Gst/s = Gt$, where $G = E/(2(1+v))$. We assume the following material properties: Young's modulus $E = 10^8$, thickness $t = 0.01$, and Poisson's ratio $v = 1/3$.

We found the stretching and shearing behavior of the hexagonal panel by assembling a stiffness matrix, applying a force of 0.5 on the top two nodes (vertical for stretching, horizontal for shearing), and solving for the nodal displacements Δ. The stiffness of the bar and hinge panel is then calculated as $K_{B\&H} = 1.0/\Delta$. Conducting this process where we systematically varied the bar areas, we found that the following definitions led to stretching and shearing behaviors that matched the theoretical solutions:

$$A_{ext} = 0.13 * t * s \qquad A_{int1} = 0.13 * 0.5 * t * s$$
$$A_{int2} = 0.13 * 60 * t * s.$$

These definitions allow the bar areas to be scaled with the side length of the hexagonal panel and panel thickness.

Appendix B. Bar area formulations for trapezoidal panels

Trapezoidal panels were modeled using the bar and hinge method with 6 bars. Four of the bars connect the nodes around the panel perimeter and two diagonal bars connect opposite corner nodes. We calculated cross-sectional areas for the bars that match the stretching and shearing behavior of the panel to the theoretical stretching and shearing of a block of material. As an additional check, we also compared the bar and hinge model results to a discretized finite element model using S4 elements. The following material properties were used for all 3 models: Young's modulus $E = 10^8$, thickness $t = 0.01$, and Poisson's ratio $v = 1/3$ (see Fig. B.1).

We started with a block of material with a height of L, thickness t, and width $W_{avg} = (W + s)/2$, where L is the length of the trapezoidal panel and W is its bottom width. We applied an upward force $F_y = 1.0$ on the top surface of the block. The resulting vertical

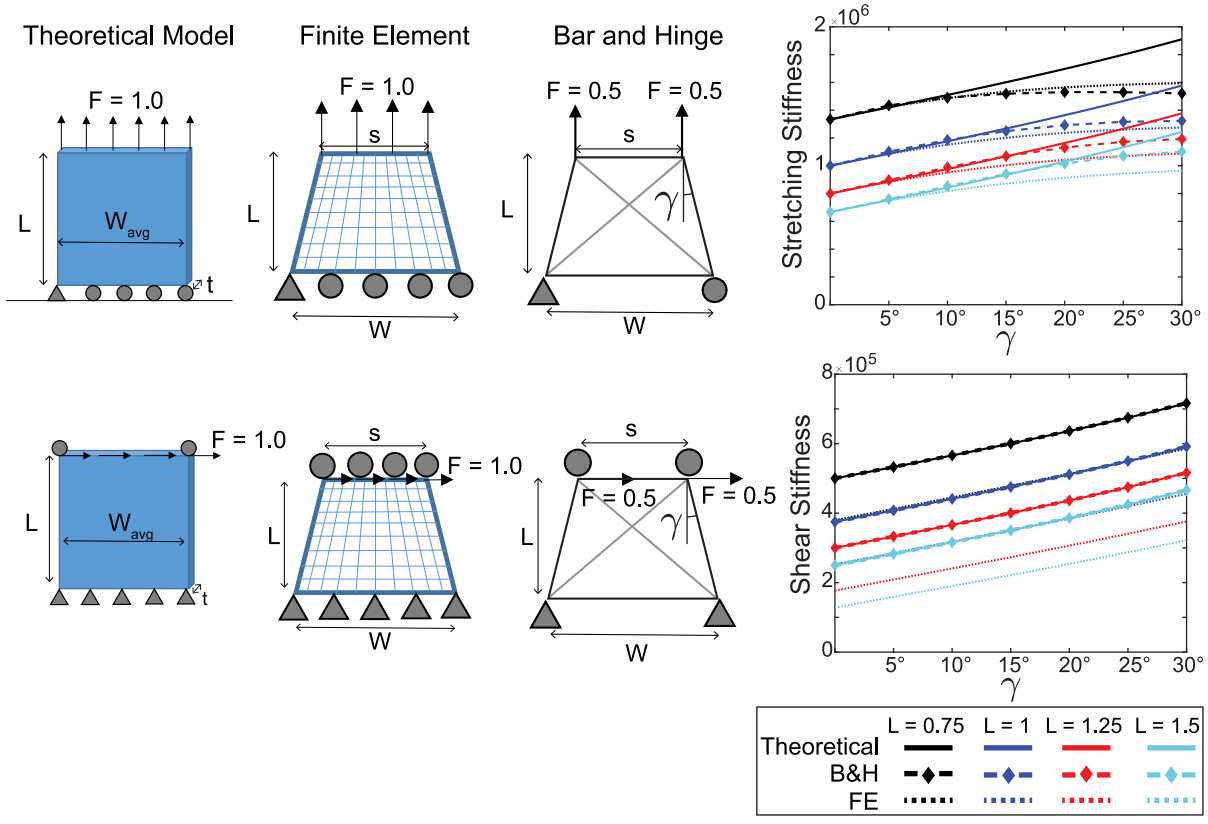

Fig. B.1. The stretching and shearing stiffness of the trapezoidal panels was defined to match the stiffness of a rectangular block of material with the same total area. The plots on the right show the performance of different models for different panel angles γ.

displacement Δ_y can be calculated using stress–strain relationships:

$$\sigma_y = \frac{F_y}{W_{avg}t} \qquad \epsilon_y = \frac{\sigma_y}{E} = \frac{F_y}{EW_{avg}t} \qquad \Delta_y = \epsilon_y L = \frac{F_y L}{EW_{avg}t}$$

The horizontal displacement Δ_x and strain ϵ_x are found using the Possion's ratio, v:

$$\Delta_x = -v\Delta_y \frac{W_{avg}}{L} \qquad \epsilon_x = \frac{\Delta_x}{W_{avg}}$$

We applied these displacements and strains to the bars of the trapezoidal panel and found the change in length Δ of each bar. Next we found the forces in each bar: $F = K\Delta = EA\Delta/L$, with the bar cross-sectional area A still unknown. From this stretching case, we obtained two independent equilibrium equations by summing the forces in the x- and y-directions at the nodes.

Using a similar process to the stretching case, we also applied a horizontal shear force to the top surface of the block of material, calculated the displacements and strains, applied them to the bars and nodes, and solved for the bar forces. The shearing case led to one additional independent equilibrium equation after summing the forces at the nodes. We obtain the fourth independent equation needed to solve for the 4 bar areas by assuming that the top and bottom bar areas are equal.

Solving the 4 equations gives expressions for the bar cross-sectional areas in terms of geometric dimensions of the trapezoid (W, L, s, t) and material parameters (E, v). The expressions for the bar areas are lengthy; we encourage interested readers to contact the authors for the full formulations. We performed a patch test to compare the behavior of the bar and hinge trapezoidal panel with the theoretical solution and a discretized FE model. The results (shown in Fig. A.1) show that the bar and hinge model with the calculated areas matches the behavior of the theoretical and FE models well. The bar and hinge model follows the same trends as the FE results, and only slightly overestimates the shear stiffness. The bar and hinge model cannot capture the local deformations that make the realistic shear case more flexible.

Appendix C. Analytical solution for stiffness of a curved sheet

The analytical solution for the stiffness of a curved sheet restrained along two edges (Fig. C.1(a)) can be calculated using Castigliano's Theorem. The theorem states that the displacement (or rotation) at a point on a beam due to a load (or moment) Q is calculated as:

$$\delta_q = \frac{\delta U}{\delta Q} = \int_0^l \frac{M}{EI}\frac{\delta M}{\delta Q}\mathrm{d}x \tag{C.1}$$

where U is the potential energy, M is the bending moment, E is the Young's modulus, and x is the distance along the beam. We can use Castigliano's Theorem in cylindrical coordinates to solve for the vertical displacement of a curved sheet due to a load applied at the centerline (Fig. C.1(a)). Due to symmetry, we look at only half of the sheet subjected to a vertical force F and compute the shear at the free end to be $V = F/2$. We consider a curved sheet with a height equal to the average clear rise of the pop-up structures (= 0.7), denoted as CR. We assume the width and length of the sheet is equal to the average clear span of the structures, CS (= 7). To transform into cylindrical coordinates, we need to relate these quantities to the radius of curvature (ρ) of the sheet (Fig. C.1(b)).

$$\rho^2 = (\rho - \mathrm{CR})^2 + \left(\frac{\mathrm{CR}}{2}\right)^2 \tag{C.2}$$

$$\rho = \frac{1}{2}\mathrm{CR} + \frac{1}{8}\frac{\mathrm{CS}^2}{\mathrm{CR}} \tag{C.3}$$

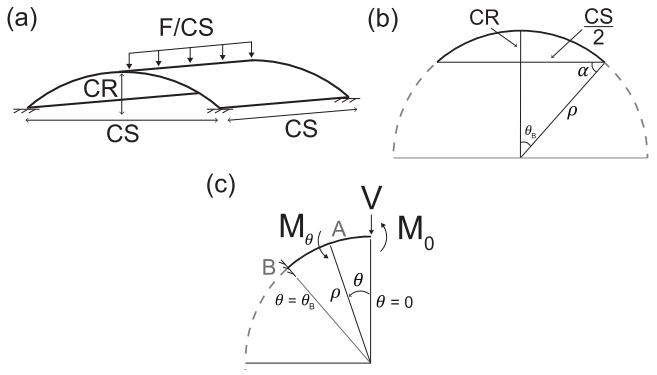

Fig. C.1. The analytical stiffness of a curved sheet used as a basepoint stiffness comparison. (a) The sheet was restrained along two edges and a load was applied at the center. (b) The sheet dimensions CR and CS, related to the radius of curvature ρ. (c) Free-body diagram of half of the curved sheet.

We need expressions for $\frac{\delta M_\theta}{\delta V}$ and $\frac{\delta M_\theta}{\delta M_0}$ to use Castigliano's Theorem, so we sum the moments at point A:

$$-M_\theta + V\rho\sin\theta - M_0 == 0 \tag{C.4}$$

$$M_\theta = V\rho\sin\theta - M_0 \tag{C.5}$$

$$\frac{\delta M_\theta}{\delta V} = \rho\sin\theta \qquad \frac{\delta M_\theta}{\delta M_0} = -1 \tag{C.6}$$

Now we can use the theorem to get an expression for the rotation due to the end moment M_0. We integrate from $\theta = 0$ to $\theta = \theta_B$, where θ_B is the angle at the support: $\theta_B = \pi/2 - \sin^{-1}((\rho - \mathrm{CR})/\rho)$. The expression for the rotation due to M_0 is

$$\begin{aligned}\delta_{M_0} &= \int_0^{\theta_B} \frac{V\rho(\sin\theta - M_0)}{EI}(-1)\rho\ \mathrm{d}\theta \\ &= \frac{V\rho^2}{EI}[\cos\theta_B - 1] + \frac{M_0\rho}{EI}\theta_B,\end{aligned} \tag{C.7}$$

and the expression for the displacement due to the end force V is

$$\begin{aligned}\delta_V &= \int_0^{\theta_B} \frac{(V\rho\sin\theta - M_0)}{EI}\rho^2\sin\theta\mathrm{d}\theta \\ &= \frac{V\rho^3}{2EI}[\theta_B - \sin\theta_B\cos\theta_B] + \frac{M_0\rho^2}{EI}[\cos\theta_B - 1].\end{aligned} \tag{C.8}$$

Due to symmetry, the rotation due to the moment M_0 is zero at the free end:

$$\frac{V\rho^2}{EI}[\cos\theta_B - 1] + \frac{M_0\rho}{EI}\theta_B = 0 \tag{C.9}$$

$$\frac{-V\rho}{\theta_B}[\cos\theta_B - 1] = M_0 \tag{C.10}$$

We can plug Equation (C.10) into Equation (C.8) to solve for the end displacement in terms of V, ρ, E, I, and θ_B, all of which are known geometric or material properties. The stiffness of the curved sheet is found using $K = F/\Delta$, where $F = 1$ and $\Delta = \delta_V$.

References

Bassik, N., Stern, G.M., Gracias, D.H., 2009. Microassembly based on hands free origami with bidirectional curvature. Applied Physics Letters 95 (9), 1–4.
Calladine, C.R., Pellegrino, S., 1991. First-order infinitesimal mechanisms. International Journal of Solids and Structures 27 (4), 505–515.
Callens, S.J., Zadpoor, A.A., 2018. From flat sheets to curved geometries: Origami and kirigami approaches. Materials Today 21 (3), 241–264.
Cho, Y., Shin, J.H., Costa, A., Kim, T.A., Kunin, V., Li, J., Lee, S.Y., Yang, S., Han, H.N., Choi, I.S., Srolovitz, D.J., 2014. Engineering the shape and structure of materials by fractal cut. Proceedings of the National Academy of Sciences 111 (49), 17390–17395.

Del Grosso, A.E., Basso, P., 2010. Adaptive building skin structures. Smart Materials and Structures 19 (12).
Demaine, E.D., Demaine, M.L., Hart, V., Price, G.N., Tachi, T., 2011. (Non)Existence of pleated folds: how paper folds between creases. Graphs and Combinatorics 27 (3), 377–397.
Demaine, E.D., Tachi, T., 2017. Origamizer: A practical algorithm for folding any polyhedron. In: 33rd International Symposium on Computational Geometry (SoCG 2017). Schloss Dagstuhl-Leibniz-Zentrum fuer Informatik. .
Dudte, L.H., Vouga, E., Tachi, T., Mahadevan, L., 2016. Programming curvature using origami tessellations. Nature Materials 15 (5), 583–588.
Feng, F., Dang, X., James, R.D., Plucinsky, P., 2020. The designs and deformations of rigidly and flat-foldable quadrilateral mesh origami. Journal of the Mechanics and Physics of Solids 142, 104018.
Filipov, E.T., Liu, K., Tachi, T., Schenk, M., Paulino, G.H., 2017. Bar and hinge models for scalable analysis of origami. International Journal of Solids and Structures 124, 26–45.
Filipov, E.T., Paulino, G.H., Tachi, T., 2019. Deployable Sandwich Surfaces with High Out-of-Plane Stiffness. Journal of Structural Engineering 145 (2), 04018244.
Filipov, E.T., Redoutey, M., 2018. Mechanical characteristics of the bistable origami hypar. Extreme Mechanics Letters 25, 16–26.
Filipov, E.T., Tachi, T., Paulino, G.H., 2015. Origami tubes assembled into stiff, yet reconfigurable structures and metamaterials. Proceedings of the National Academy of Sciences 112 (40), 12321–12326.
Fonseca, N.J., Girard, E., Legay, H., 2018. Doubly curved reflector design for hybrid array fed reflector antennas. IEEE Transactions on Antennas and Propagation 66 (4), 2079–2083.
Girija Vallabhan, C.V., Panneer Selvam, R., 1985. A Computer model for stress analysis of spherically curved solar panels. Journal of Solar Energy Engineering, Transactions of the ASME 107 (4), 281–285.
Hawkes, E., An, B., Benbernou, N.M., Tanaka, H., Kim, S., Demaine, E.D., Rus, D., Wood, R.J., 2010. Programmable matter by folding. Proceedings of the National Academy of Sciences 107 (28), 12441–12445.
Huerta, S., 2007. Oval domes: History, geometry and mechanics. Nexus Network Journal 9 (2), 211–248.
Kangwai, R., Guest, S., 1999. Detection of finite mechanisms in symmetric structures. International Journal of Solids and Structures 36 (36), 5507–5527.
Kuribayashi, K., Tsuchiya, K., You, Z., Tomus, D., Umemoto, M., Ito, T., Sasaki, M., 2006. Self-deployable origami stent grafts as a biomedical application of ni-rich tini shape memory alloy foil. Materials Science and Engineering: A 419 (1–2), 131–137.
Lang, R.J., Tolman, K.A., Crampton, E.B., Magleby, S.P., Howell, L.L., 2018. A review of thickness-accommodation techniques in origami-inspired engineering. Applied Mechanics Reviews 70 (1), 1–20.
Lee, T.-U., Gattas, J.M., 2016. Geometric design and construction of structurally stabilized accordion shelters. Journal of Mechanisms and Robotics 8 (3).
Leong, T.G., Benson, B.R., Call, E.K., Gracias, D.H., 2008. Thin film stress driven self-folding of microstructured containers. Small 4 (10), 1605–1609.
Liu, K., Paulino, G.H., 2017. Nonlinear mechanics of non-rigid origami: An efficient computational approach. Proceedings of the Royal Society A: Mathematical, Physical and Engineering Sciences 473 (2206).
Liu, K., Paulino, G.H., 2018. Highly efficient nonlinear structural analysis of origami assemblages using the MERLIN2 software. Origami 7, 1167–1182.
Maker, J., 2017. Penguin paper bomb. https://jennifermaker.com/penguin-paper-bomb/. .
Martin, A.G., 2015. A basketmaker's approach to structural morphology. Proceedings of the International Association for Shell and Spatial Structures (IASS), (August). .
Massey, W.S., 1962. Surfaces of gaussian curvature zero in euclidean 3-space. Tohoku Mathematical Journal, Second Series 14 (1), 73–79.
Modes, C.D., Bhattacharya, K., Warner, M., 2011. Gaussian curvature from flat elastica sheets. Proceedings of the Royal Society A: Mathematical, Physical and Engineering Sciences 467 (2128), 1121–1140.
Nakamura, H., 2016. Karakuri Kamikara. Nihon Bungeisha.
Nojima, T., Saito, K., 2006. Development of newly designed ultra-light core structures. JSME International Journal Series A Solid Mechanics and Material Engineering 49 (1), 38–42.
Pedreschi, R., Theodossopoulos, D., 2007. The double-curvature masonry vaults of Eladio Dieste. Proceedings of the Institution of Civil Engineers: Structures and Buildings 160 (1), 3–11. .
Pellegrino, S., 1988. On the rigidity of triangulated hyperbolic paraboloids. Proceedings of The Royal Society of London, Series A: Mathematical and Physical Sciences 418 (1855), 425–452.
Pellegrino, S., 1992. A class of tensegrity domes. International Journal of Space Structures 7 (2), 127–142.
Pellegrino, S., Calladine, C.R., 1986. Matrix analysis of statically and kinematically indeterminate frameworks. International Journal of Solids and Structures 22 (4), 409–428.
Pini, V., Ruz, J.J., Kosaka, P.M., Malvar, O., Calleja, M., Tamayo, J., 2016. How two-dimensional bending can extraordinarily stiffen thin sheets. Scientific Reports 6 (July), 1–6.
Schenk, M., Guest, S.D., 2013. Geometry of Miura-folded metamaterials. Proceedings of the National Academy of Sciences 110 (9), 3276–3281.
Schenk, M., Guest, S.D., 2016. Origami folding: A structural engineering approach. In: Origami 5: Fifth International Meeting of Origami Science, Mathematics, and Education, pp. 291–303. .
Tachi, T., 2010. Origamizing polyhedral surfaces. IEEE Transactions on Visualization and Computer Graphics 16 (2), 298–311.
Tachi, T., 2016. Rigid-foldable thick origami. In: Origami 5: Fifth International Meeting of Origami Science, Mathematics, and Education, pp. 253–263. .
Tarnai, T., 2001. Infinitesimal and Finite Mechanisms. Springer Vienna, pp. 113–142.
Thrall, A.P., Quaglia, C.P., 2014. Accordion shelters: A historical review of origami-like deployable shelters developed by the US military. Engineering Structures 59, 686–692.
Tibert, A.G., Pellegrino, S., 2002. Deployable tensegrity reflectors for small satellites. Journal of Spacecraft and Rockets 39 (5), 701–709.
Wulfrank, T., Jurkiewicz, Y., Kahle, E., 2014. Design-focused acoustic analysis of curved geometries using a differential raytracing technique. Building Acoustics 21 (1), 87–95.
Yuan, X., Chen, L., Dong, S., 2007. Prestress design of cable domes with new forms. International Journal of Solids and Structures 44 (9), 2773–2782.
Zhang, Y., Yan, Z., Nan, K., Xiao, D., Liu, Y., Luan, H., Fu, H., Wang, X., Yang, Q., Wang, J., Ren, W., Si, H., Liu, F., Yang, L., Li, H., Wang, J., Guo, X., Luo, H., Wang, L., Huang, Y., Rogers, J.A., 2015. A mechanically driven form of Kirigami as a route to 3D mesostructures in micro/nanomembranes. Proceedings of the National Academy of Sciences 112 (38), 11757–11764.
Zhu, Y., Birla, M., Oldham, K.R., Filipov, E.T., 2020. Elastically and plastically foldable electrothermal micro-origami for controllable and rapid shape morphing. Advanced Functional Materials 2003741, 1–10.
Zhu, Y., Filipov, E.T., 2019. An efficient numerical approach for simulating contact in origami assemblages. Proceedings of the Royal Society A 475 (2230), 20190366. .
Zirbel, S.A., Lang, R.J., Thomson, M.W., Sigel, D.A., Walkemeyer, P.E., Trease, B.P., Magleby, S.P., Howell, L.L., 2013. Accommodating thickness in origami-based deployable arrays1. Journal of Mechanical Design, Transactions of the ASME 135 (11), 1–11.
Zirbel, S.A., Trease, B.P., Thomson, M.W., Lang, R.J., Magleby, S.P., Howell, L.H., 2015. HanaFlex: a large solar array for space applications. Micro- and Nanotechnology Sensors, Systems, and Applications VII 9467 (May 2015), 94671C. .